Investigation of the equivalent mechanical properties of the bone-inspired composite cellular structure: Analytical, numerical and experimental approaches

Fatemeh Ghorbani[1], Hussain Gharehbaghi[1], Amin Farrokhabadi[*1], Amir Bolouri[2]

[1] Department of Mechanical Engineering, Tarbiat Modares University, Tehran, Iran.

[2] School of Engineering, University of the West of England, Bristol, UK.

Abstract

This study investigated the development of an analytical model using the energy method and Castigliano's second theory to evaluate the equivalent mechanical properties for a bone-inspired cellular structure of a glass fiber-reinforced Polylactic Acid (PLA) composite material. The bone-inspired cellular structure was fabricated using a Fused Deposition Modeling (FDM) 3D printing technique. The fabricated specimens were subjected to compression testing. The digital image correlation technique was employed for obtaining stain and displacement contours in experimental tests. Furthermore, a finite element numerical model was developed to evaluate the mechanical properties of the bone-inspired composite cellular structure. The comparison of the experimental and numerical results with the outcomes of analytical model revealed that the proposed analytical model can correctly determine the mechanical properties of the composite bio-inspired cellular structure. The results showed that by reinforcing the cellular structure with continuous fiber, significantly higher mechanical properties can be obtained. A comprehensive parametric study has also been performed to investigate the effect of geometric parameters on equivalent mechanical properties.

Keywords: Digital Image Correlation (DIC), Fiber reinforced cellular structure, Classical lamination theory (CLT), energy method

[*] Corresponding Author, Email Address: amin-farrokh@modares.ac.ir

1.Introduction

Cellular structures have significant mechanical properties and are widely used in lightweight applications. These structures are often used in aerospace, civil engineering, transportation, medical engineering, and sports engineering because of their useful properties [1],[2]. Their applications include energy absorption [3], heat exchangers[4], acoustic[5], vibration damping[6], and bio-implant design[7]. Today, with the development of 3D printers, it is possible to fabricate complex cellular structures and perform experimental tests to evaluate the performance of analytical and numerical results.

Various methods for studying the mechanical properties of two-dimensional and three-dimensional cellular structures have been used in several studies. Naghavizadeh et al. [8], [9] evaluated in-plane mechanical properties in a novel 2D dimensional fish cell structure, using Castigliano's second theorem and energy method. They assessed the analytical model using a numerical method based on homogenization and performed an experimental test. Babaee et al. [10] employed the energy method to obtain the in-plane elastic modulus in the open rhomboidal dodecahedron unit cell analytically. Then, they analyzed the results of the analytical model using finite element analysis. Harakati et al. [11] investigated the multi-entrant structure's in-plane mechanical properties analytically and employed the finite element analysis based on homogenization to investigate the accuracy of the analytical model. The finite element analysis results showed a good agreement with the theoretical model. Lira et al. [12] analyzed the out-of-plane shear properties in the novel multi-re-entrant honeycomb cell structure based on Voigt and Reuss bounds. Masters and Evans [13] developed an analytical model to obtain the mechanical properties of honeycomb structure under bending, tensile, and hinge deformation. Lu et al. [14] developed an analytical model for obtaining the Poisson's ratio and Young's modulus in a novel structure inspired by the conventional honeycomb and re-entrant cellular structures. The results showed that the proposed structure has high Young's modulus than conventional structures. Liu et al. [15] theoretically presented the in-plane mechanical properties of the corrugated cosine cell structure, then validated their results using a numerical simulation based on periodic boundary conditions. Rong and Zhou [16] investigated the in-plane mechanical properties of the cruciform honeycomb structure analytically and experimentally. Li et al. [17] presented an analytical model based on four different geometric parameters in the three-dimensional re-entrant lattice structure

under compressive loading to obtain the Poisson's ratio, failure mode, failure strength, and effective modulus. Results showed that the analytical model has good agreement with the experimental tests and numerical analysis. Torre et al. [18] have investigated the effective parameters in printing polymeric elements in FFF 3D printers. The results demonstrated that a 100% linear infill reduced the anisotropy response of printed components.

Some studies considered the effect of cell topologies on the mechanical performance of honeycomb structures using a titanium alloy and a flexible polymer []. Also, the surface quality is investigated as the important key in their research. Results demonstrated that the gradual change in the topology of the honeycomb unit cell can result in a higher deformation energy.

Oftadeh et al. [19] proposed a theoretical model based on Castigliano's second theorem for the hierarchical honeycomb structure. Using the presented model, they obtained the elastic modulus, Poisson's ratio, shear modulus, and plastic collapse strength and evaluated their results using a numerical method. Liu et al. [20] studied the two-dimensional chiral structure, which consists of four V-shaped elements. The analytical model was done using the energy method, and the finite element analysis was employed to validate the results. Huang et al. [21] presented the in-plane mechanical properties of the novel honeycomb core with a zero Poisson's ratio theoretically based on Castigliano's second theorem. The obtained results were evaluated using numerical simulation and experimental tests. Wang and Deng [22] presented the in-plane mechanical properties in the x and y directions, including Young's modulus and the Poisson's ratio in the irregular honeycomb cell structure using Castigliano's theorem. Mukhopadhyay and Adhikari [23] extended an analytical model for obtaining the equivalent in-plane mechanical properties in an auxetic honeycomb structure with special irregularity and investigated the effect of irregularities in the proposed structure on the Poisson's ratio, shear modulus, and elastic modulus. Liu et al. [24] proposed a novel cellular structure for morphing structures application. They studied the in-plane and out-of-plane mechanical properties of structure, analytically and numerically. Gong et al. [25] proposed another novel honeycomb structure applicable for morphing structures. They presented in-plane and out-of-plane mechanical properties using Castigliano's theorem and investigated the results by using finite element analysis. Balawi and Abot [26] studied the in-plane mechanical properties in the honeycomb structure with curved struts. They used the energy method to obtain the mechanical properties analytically and assessed the results by employing the finite element method. Harkati et al. [27] extended an

analytical theory to obtain the in-plane elastic properties of the honeycomb structure with curved struts. In the proposed model, they applied Castigliano's second theorem and validated the results using the finite element analysis. Employing the Euler-Bernoulli beam theory, Gao et al. [28] extended an analytical model to obtain the mechanical properties of the cylindrical double arrowed honeycomb structure (DHS). They used the finite element method to validate the proposed theoretical model. The results show that the proposed model in a large radius cannot correctly calculate the elastic mechanical properties. Ghazlan et al. [29][30] presented the elastic modulus of a bone-inspired cellular structure using the stiffness matrix method. They assessed their results using experimental tests. Hedayati et al. [31] extended two analytical models based on Euler-Bernoulli and Timoshenko beam theory and compared them in six different unit cells. Results showed that the Timoshenko beam theory is more consistent with finite element analysis results than the Euler-Bernoulli beam theory.

Torre et al. [32] have investigated the behavior of short-length PLA 3D printed samples under compression with a specific focus on the buckling. The square polymeric columns were produced by Fused Filament Fabrication (FFF) and utilized in experimental tests. The compression of the specimens was monitored using a single-camera Digital Image Correlation (DIC) system, and the slenderness ratio at which the elements started to buckle was identified. The experimental results were compared with analytical, linear, and non-linear Finite Elements (FE) models.

Quan et al. [33] fabricated the re-entrant structure, which was reinforced with Kevlar fibers using FDM technology, and studied the in-plane compression behavior. They also performed an analytical model for obtaining the elastic modulus and Poisson's ratio. They validated their analytical and numerical results using experimental tests. Veisi and Farrokhabadi [34] presented a new analytical model based on the classical lamination theory (CLT) to evaluate the in-plane mechanical properties of the fiber-reinforced re-entrant structure. They compared their results with the available finite element analysis and experimental tests mentioned in previous studies. The results showed that the proposed analytical model has good agreement with numerical and experimental results. Farrokhabadi et al. [35] studied the fiber-reinforced cruciform unit cell. They studied the mechanical properties of the proposed structure under tensile loading. Castigliano's second theorem and energy method were employed in their theoretical model. They

evaluated their results using experimental tests and numerical analysis. Farrokhabadi et al. [36] presented a novel analytical model to evaluate the mechanical properties of the fiber-reinforced U-type unit cell. They have used experimental tests and numerical analysis under tensile loading to validate the proposed theoretical model.

Reviewing the previous studies, it can be understood that the bone-inspired unit cell has better mechanical properties than conventional honeycomb and re-entrant structures[30]. This feature can be employed for design of lightweight structures. In this study, a novel composite bone-inspired cellular structure is designed for lightweight applications. This composite structure is fabricated with a continuous glass fiber and polylactic acid using the FDM 3D printer. Furthermore, an analytical model based on the energy method and classical lamination theory (CLT) is proposed to investigate the equivalent mechanical properties in a bone-inspired cellular structure with composite struts. This novel approach provides an equivalent model that use the geometric parameters of the composite bone-inspired unit cell as variables and calculates equivalent mechanical properties. The analytical model is validated using numerical simulation and experimental tests. In addition, Digital Image Correlation (DIC) technique has been used to investigate the in-plane strains. Finally, the effect of geometrical parameters of the cellular structure on equivalent mechanical properties is studied.

2. The bone-inspired cellular structure

Bone is made up of cancellous and cortical tissue (Fig.1). Cancellous bone consists of interconnected rods and plates. These features create the unique low-weight and high-strength properties of bone.

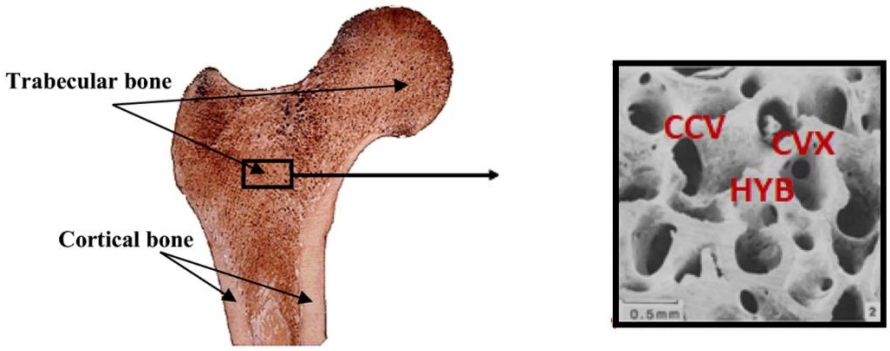

Figure1. Cancellous bone structure.

The structural arrangement in cancellous bone created a porous area that can indicate different cellular structure patterns including concave, convex, or hybrid cells (Fig. 1). In the bone, which has osteoporosis condition the porosity of this area becomes bigger and the cells may have different sizes. The bone-inspired cellular structure is introduced based on the hybrid design of cancellus bone in [29], [30] and contained two different sub-cells. Fig.2 represents a schematic architecture of a bone-inspired cellular structure and the geometrical parameters of its unit cell. For a composite bio-inspired cellular structure, the isotropic and orthotropic mechanical properties in different directions are calculated based on the following sections.

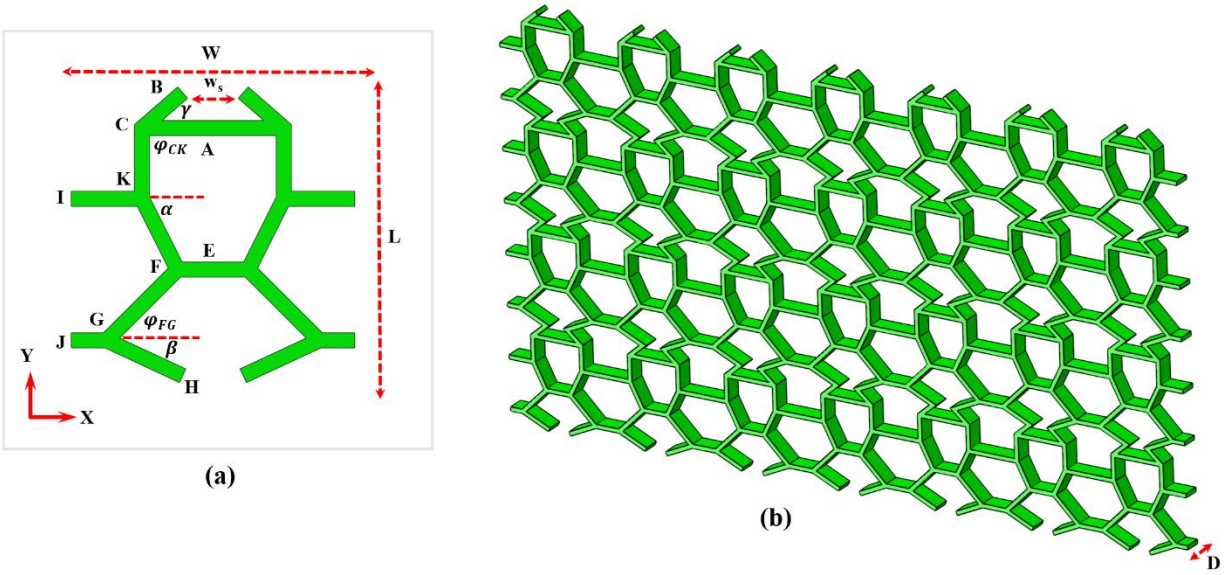

Figure 2. (a) The bone inspired unit cell with geometrical parameters and (b) a bone-inspired cellular structure.

3. Elastic properties

3.1. Elastic properties in an orthotropic ply with unidirectional fibers

The energy method and Castigliano's second theorem have been used to calculate the in-plane elastic properties of the orthotropic laminated cellular structure shown in Fig.3. According to the

classical lamination theory (CLT), the constitutive equation of an orthotropic ply in the global coordinate system is extracted as Eq.1 under the plane stress condition.

$$\begin{bmatrix}\sigma_{xx}\\ \sigma_{yy}\\ \sigma_{xy}\end{bmatrix}=\begin{bmatrix}\bar{Q}_{11} & \bar{Q}_{12} & \bar{Q}_{16}\\ \bar{Q}_{12} & \bar{Q}_{22} & \bar{Q}_{26}\\ \bar{Q}_{16} & \bar{Q}_{26} & \bar{Q}_{66}\end{bmatrix}\begin{bmatrix}\varepsilon^0_{xx}+z\kappa^0_{xx}\\ \varepsilon^0_{yy}+z\kappa^0_{yy}\\ \Upsilon^{\,0}_{xy}+z\kappa^0_{xy}\end{bmatrix} \quad \text{(Eq. 1)}$$

Where $[\bar{Q}]$ is the transformed reduced stiffness matrix, ε^0_{xx}, ε^0_{yy} and Υ^0_{xy} are midplane strain components and κ^0_{xx}, κ^0_{yy} and κ^0_{xy} are the midplane curvatures. Fig.3 shows the axial forces and bending moments resultants in an orthotropic ply, in which the fiber is align with the x-direction. The total strain energy in an orthotropic ply is obtained as Eq.2.

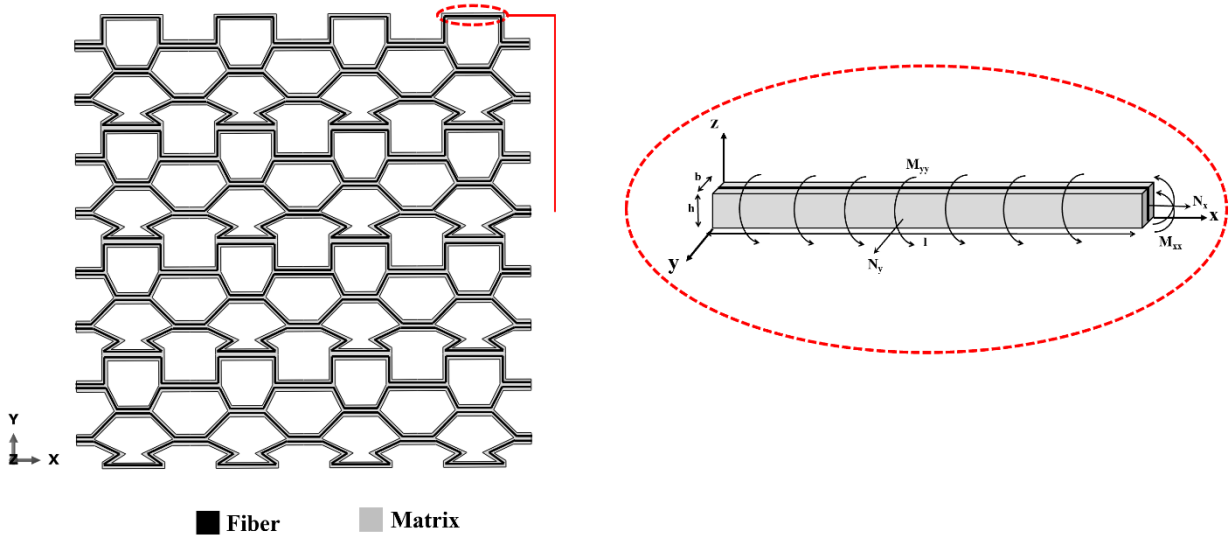

Figure 3. Forces and moments resultants in an orthotropic ply

$$U_{tot}=U_{axial}+U_{bending} \quad \text{(Eq. 2)}$$

Under the presented applied loading, the axial strain energy of an orthotropic ply can be written as Eq.3.

$$U_{axial}=\frac{1}{2}\int_V(\sigma_{xx}\varepsilon_{xx}+\sigma_{yy}\varepsilon_{yy})\,dV \quad \text{(Eq.3)}$$

Where σ_{xx} and ε_{xx} are axial stress and strain in the x-direction, σ_{yy} and ε_{yy} are the axial stress and strain in the y-direction. Forces and moments resultants in Fig.3 can be obtained as Eqs.4a-d.

$$N_x = \int_{-\frac{h}{2}}^{\frac{h}{2}} \sigma_{xx}\, dz \quad \text{(Eq.4-a)}$$

$$N_y = \int_{-\frac{h}{2}}^{\frac{h}{2}} \sigma_{yy}\, dz \quad \text{(Eq.4-b)}$$

$$M_{xx} = \int_{-\frac{h}{2}}^{\frac{h}{2}} \sigma_{xx} z dz \quad \text{(Eq.4-c)}$$

$$M_{yy} = \int_{-\frac{h}{2}}^{\frac{h}{2}} \sigma_{yy} z dz \quad \text{(Eq.4-d)}$$

It is worth noting that midplane curvatures are zeros in the axial loading, so by considering Eq.3 and employing Eqs.4a-d, the axial strain energy can be obtained as Eq.5.

$$U_{axial} = \frac{1}{2}\int_V (\sigma_{xx}\varepsilon_{xx}^0 + \sigma_{yy}\varepsilon_{yy}^0) dV = \frac{1}{2}\int_0^l \int_0^b (N_x\, \varepsilon_{xx}^0 + N_y \varepsilon_{yy}^0) dx dy \quad \text{(Eq.5)}$$

The force resultants are defined as $N_x = \frac{F_x}{b}$ and $N_y = \frac{F_y}{l}$.

To obtain the bending strain energy relation, the strain components are defined as Eqs.6a and b.

$$\varepsilon_{xx} = z\kappa_{xx}^0 = z\frac{M_{xx}}{E_{11} I_{yy}} \quad \text{(Eq. 6-a)}$$

$$\varepsilon_{yy} = z\kappa_{yy}^0 = z\frac{M_{yy}}{E_{22} I_{xx}} \quad \text{(Eq.6-b)}$$

Where, I_{xx} and I_{yy} are second moment of inertia about x and y axes, respectively. The resultant moments are considered as $M_x = \frac{M_{xx}}{b}$ and $M_y = \frac{M_{yy}}{l}$, so the bending strain energy is obtained as Eq.7.

$$U_{bending} = \frac{1}{2}\left(\int_0^l \frac{M_{xx}^2}{E_{11} I_{yy}} dx + \int_0^b \frac{M_{yy}^2}{E_{22} I_{xx}} dy\right) \quad \text{(Eq.7)}$$

As a result, for an orthotropic ply, the total strain energy in a global coordinate system can be derived as Eq.8.

$$U_{tot} = \frac{1}{2}\left(\int_0^l \frac{F_x^2 l}{A_x E_{11}} dx + \int_0^b \frac{F_y^2 b}{A_y E_{22}} dy + \int_0^l \frac{M_{xx}^2}{E_{11} I_{yy}} dx + \int_0^b \frac{M_{yy}^2}{E_{22} I_{xx}} dy\right) \quad \text{(Eq.8)}$$

3.2. Calculation of elastic properties in the x-direction

Using the theory presented in the previous section and Castigliano's second theorem, the elastic properties of the bio-inspired unit cell in the x-direction are calculated in this section. The deformation of the unit cell is investigated by applying x-direction tensile loading to the tessellation, which is constructed by several unit cells. By observing the deformation in the tessellation, boundary conditions for a unit cell are extracted. Due to symmetry, half of the unit cell has been studied. The free diagram of the bio-inspired unit cell is shown in Fig.4.

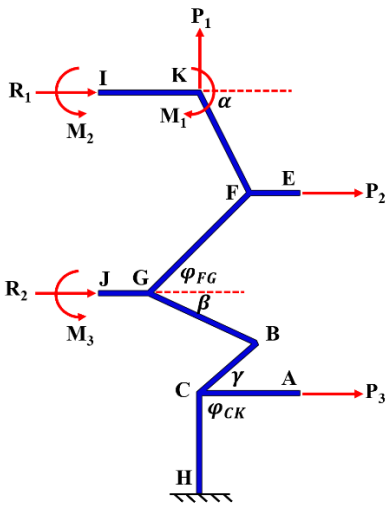

Figure 4. Free digram of half of the unit cell under loading x-direction

In this figure, R_1 and R_2 are reactions forces, P_2 and P_3 are the forces acting in the x-direction, P_1 indicates the virtual force acting in the y-direction to obtain lateral displacement, and M_1, M_2 and M_3 represents the reaction moments at points K, I, J. While, the lengths of the struts KF, FG, GB, BC, and CH are considered L, the length of KI = B_1, GJ = B_2, FE = C_1, and CA = C_2 are considered L/2. In addition, $\alpha = 2\beta$, $\gamma = 2\beta$, $\varphi_{FG} = 2\beta$, $\varphi_{CK} = 3\beta$. The internal forces and moments are obtained by writing the equilibrium equation at each strut of the unit cell and presented in Eqs.9a, and b.

$$
\begin{aligned}
&F_{KI} = -R_1 \\
&F_{KF} = P_1\, sin\alpha - R_1\, cos\alpha \\
&F_{FE} = P_2 \\
&F_{FG} = P_1\, sin\varphi_{fg} + (R_1 + P_2) cos\varphi_{fg} \\
&F_{GJ} = -R_2 \\
&F_{GB} = P_1\, sin\beta - (R_1 + P_2 + R_2\,) cos\beta \\
&F_{BC} = P_1\, sin\gamma + (R_1 + P_2\ + R_2) cos\gamma \\
&F_{CA} = P_3 \\
&F_{CH} = P_1
\end{aligned}
\quad \text{(Eqs.9a)}
$$

$$
\begin{aligned}
&M_{KI} = M_2 \\
&M_{KF} = M_1 - M_2 + (P_1 cos\alpha + R_1 sin\alpha)x \\
&M_{FE} = 0 \\
&M_{FG} = M_1 - M_2 + (P_1 cos\alpha + R_1 sin\alpha)L + ((R_1 + P_2) sin\varphi_{fg} - P_1 cos\varphi_{fg})x \\
&M_{GJ} = M_3 \\
&M_{GB} = M_1 - M_2 - M_3 + \Big((P_1 cos\alpha + R_1 sin\alpha) + (R_1 + P_2) sin\varphi_{fg} - P_1 cos\varphi_{fg}\Big) L + (R_1 sin\beta + \\
&(P_1 + P_2 + R_2) cos\beta)x \\
&M_{BC} = M_1 - M_2 - M_3 + ((P_1 cos\alpha + R_1 sin\alpha) - P_1 cos\varphi_{fg} + (R_1 + P_2) sin\varphi_{fg} + R_1 sin\beta + \\
&(P_1 + P_2 + R_2) cos\beta)L \\
&+\big((R_1 + P_2 + R_2) sin\gamma - P_1 cos\gamma\big)x \\
&M_{CA} = 0 \\
&M_{CH} = M_1 - M_2 - M_3 + (P_1 cos\alpha + R_1 sin\alpha) - \big(P_1 cos\varphi_{fg} + (R_1 + P_2) sin\varphi_{fg} + R_1 sin\beta + \\
&(P_1 + P_2 + R_2) cos\beta - P_1 cos\gamma + (R_1 + P_2 + R_2) sin\gamma\big)L + (R_1 + P_2 + R_2 + P_3)x
\end{aligned}
\quad \text{(Eqs.9b)}
$$

By calculating the internal forces and moments in each strut of the unit cell and substituting them in Eq.8, the axial and bending strain energies are obtained as Eqs.10a and b. While the located fibers in diagonal struts are not capable to transform the applied compressive loading, the mechanical properties of the pure PLA are assigned for these struts. Meanwhile, for all the straight struts, the elastic modulus is considered E_{11}. For the straight struts, the thicknesses are

double and their cross-section area and moment of inertia are considered as A_{2t} and I_2, respectively. For other struts, the cross-section area and moment of inertia are considered as A_t and I_1, respectively.

$$U_{axial} = \frac{1}{2E_s A_t}\left[\int_0^L {F_{KF}}^2 + \int_0^L {F_{FG}}^2 + \int_0^L {F_{GB}}^2 + \int_0^L {F_{BC}}^2 + \int_0^L {F_{CH}}^2\right] dx + \frac{1}{2E_{11}A_{2t}}\left[\int_0^{\frac{L}{2}} {F_{KI}}^2 + \int_0^{\frac{L}{2}} {F_{GJ}}^2 + \int_0^{\frac{L}{2}} {F_{FE}}^2 + \int_0^{\frac{L}{2}} {F_{CA}}^2\right] dx \quad \text{(Eq. 10a)}$$

$$U_{bending} = \frac{1}{2E_s I_1}\left[\int_0^L {M_{KF}}^2 + \int_0^L {M_{FG}}^2 + \int_0^L {M_{GB}}^2 + \int_0^L {M_{BC}}^2 + \int_0^L {M_{CH}}^2\right] dx + \frac{1}{2E_{11}I_2}\left[\int_0^{\frac{L}{2}} {M_{KI}}^2 + \int_0^{\frac{L}{2}} {M_{GJ}}^2\right] dx \quad \text{(Eq. 10b)}$$

By calculating the axial force and bending moment using Eqs.9a and b and substituting them into Eqs.10a and b, the total strain energies can be calculated. The displacement in the x-direction (δ_x) is obtained by applying the total strain energy and Castigliano's theorem at the P_2 or P_3. The equivalent elastic modulus in the x-direction is obtained using Hooke's law and presented in Eq.11. Supplementary equations can be found in Maple file provided for the calculations in x-direction.

$$E_x = F(E_s, E_{11}, L, H, W, D, t, \beta) \quad \text{(Eq.11)}$$

3.3. Calculation of elastic properties in the y-direction

In this section, same as the x-direction, Castigliano's second theorem theory was used to calculate the elastic properties of the bio-inspired unit cell in the y-direction. By applying a tensile load in the y-direction in tessellation, the deformation of a unit cell is obtained, and the boundary conditions are extracted. Due to symmetry, half of the unit cell was considered. The free diagram of half the unit cell is shown in Fig.5.

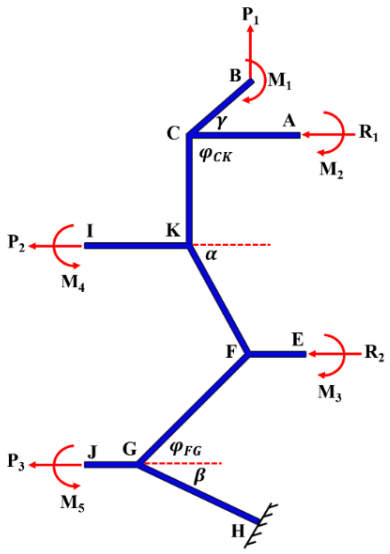

Figure 5. Free digram of half of the unit cell under loading y-direction

In this figure R_1 and R_2 are considered as the reaction loads, P_2 and P_3 indicate the virtual forces acting in the x-direction to obtain lateral displacement, P_1 is the force acting in the y direction, and M_1, M_2, M_3, M_4, M_5 represent the reaction moments at points B, A, E, I, J, respectively. The length of the struts BC, CK, KF, FG, GH are considered L and the length of struts CA = B_1, FE = B_2, KI = C_1 and GJ = C_2 are considered L/2. In addition, it is considered that $\alpha = 2\beta$, $\gamma = 2\beta$, $\varphi_{FG} = 2\beta$, $\varphi_{CK} = 3\beta$. Internal forces and moments are obtained by writing the equilibrium equation in every strut from the unit cell and presented in Eqs.12a and b.

$$
\left.
\begin{aligned}
F_{BC} &= P_1 sin\gamma \\
F_{CA} &= -R_1 \\
F_{CK} &= P_1 + R_1 cos\varphi_{cd} \\
F_{KI} &= P_2 \\
F_{KF} &= P_1 sin\alpha + (R_1 + P_2) cos\alpha \\
F_{FE} &= -R_2 \\
F_{FG} &= P_1 sin\varphi_{fg} - (R_1 + P_2 + R_2) cos\varphi_{fg} \\
F_{GJ} &= P_3 \\
F_{GH} &= P_1 sin\beta + (R_1 + P_2 + R_1 + P_3) cos\beta
\end{aligned}
\right\} \text{(Eqs.12a)}
$$

$$
\begin{aligned}
&M_{BC} = M_1 - P_1 x cos\gamma \\
&M_{CA} = M_2 \\
&M_{CK} = M_1 + M_2 - P_1 L cos\gamma - R_1 x \\
&M_{KI} = M_4 \\
&M_{KF} = M_1 + M_2 - M_4 - (P_1 cos\gamma + R_1)\mathrm{L} + (P_1 cos\alpha - (P_2 + R_1) sin\alpha)x \\
&M_{FE} = M_3 \\
&M_{FG} = M_1 + M_2 + M_3 - M_4 - (P_1 cos\gamma + R_1 - P_1 cos\alpha + (P_2 + R_1) sin\alpha)L - \big(P_1 cos\varphi_{fg} + \\
&(R_1 + P_2 + R_2) sin\varphi_{fg}\big)x \\
&M_{GJ} = M_5 \\
&M_{GH} = M_1 + M_2 + M_3 - M_4 - \big(P_1 L_1 cos\gamma + R_1 + P_1 cos\alpha + (P_2 + R_1) sin\alpha + P_1 cos\varphi_{fg} + \\
&(R_1 + P_2 + R_2) sin\varphi_{fg}\big)L + (P_1 cos\beta - (R_1 + R_2 + P_2) sin\beta)x
\end{aligned}
\quad \text{(Eqs.12b)}
$$

After calculating the internal forces and moments in each strut of the unit cell, the axial and bending strain energies can be written as Eqs.13a, and b. In the diagonal struts, the mechanical properties are assumed to be E_s, and in the remain straight struts, it is considered to be E_{11}. In the straight struts, the thicknesses are double. Furthermore, cross-section area and moment of inertia in the straight struts are considered A_{2t} and I_2, respectively. In other struts, they are considered A_t and I_1, respectively.

$$
U_{axial} = \frac{1}{2E_s A_t}\left[\int_0^L {F_{BC}}^2 + \int_0^L {F_{CK}}^2 + \int_0^{\mathrm{L}} {F_{KF}}^2 + \int_0^{\mathrm{L}} {F_{FG}}^2 + \int_0^L {F_{GH}}^2\right] dx + \frac{1}{2E_{11}A_{2t}}\left[\int_0^{\frac{L}{2}} {F_{CA}}^2 + \int_0^{\frac{L}{2}} {F_{FE}}^2 + \int_0^{\frac{L}{2}} {F_{KI}}^2 + \int_0^{\frac{L}{2}} {F_{GJ}}^2\right] dx \quad \text{(Eq.13-a)}
$$

$$
U_{bending} = \frac{1}{2E_s I_1}\left[\int_0^L {M_{BC}}^2 + \int_0^L {M_{CK}}^2 + \int_0^L {M_{KF}}^2 + \int_0^L {M_{FG}}^2 + \int_0^L {M_{GH}}^2\right] dx + \frac{1}{2E_{11}I_2}\left[\int_0^{\frac{L}{2}} {M_{CA}}^2 + \int_0^{\frac{L}{2}} {M_{FE}}^2\right] dx \quad \text{(Eq.13-b)}
$$

The y-direction axial forces and bending moments which are evaluated using Eqs.12a and b are substitute in Eqs.13a and b to obtain the total strain energy. The displacement in the y-direction (δ_y) can be obtained by applying the total strain energy and Castigliano's theorem at the P_1. Accordingly, the equivalent elastic modulus in the y-direction is obtained using Hooke's law and

presented in Eq.14. Supplementary equations can be found in Maple file provided for the calculations in y-direction.

$$E_y = F(E_s, E_{11}, L, H, W, D, t, \beta) \quad \text{(Eq.14)}$$

Poisson's ratio is defined as the ratio of lateral strain to longitudinal strain. To obtain the Poisson's ratio, virtual loads i.e., P_2 and P_3 are imposed for lateral displacement (Fig.5). The lateral displacement in the x-direction is calculated using Castigliano's second theorem and differentiation of the total strain energy to the P_2 or P_3. Having the displacement in the y-direction the major Poisson's ratio (υ_{xy}) can be evaluated as Eq.15.

$$\upsilon_{xy} = -\frac{\varepsilon_x}{\varepsilon_y} \quad \text{(Eq.15)}$$

Furthermore, υ_{yx} can be obtained using the Maxwell theory, as Eq.16.

$$\upsilon_{yx} = \frac{\upsilon_{xy} E_y}{E_x} \quad \text{(Eq.16)}$$

4. Experimental method

4.1. Materials and samples fabrication

For experimental testing, composite specimens were manufactured using an FDM 3D printer. Polylactic acid (PLA) filament (the matrix material) and continuous E-glass fiber (the reinforcing material) were used. Fig.6a shows a composite bio-inspired cellular structure manufactured using the FDM 3D printer. As shown in Fig 6, a continuous glass fiber is located in the direction of the struts of the unit cell and comes out of the nozzle with the PLA matrix simultaneously.
The mechanism of the manufacturing method is shown in Fig.6b. A special nozzle has been designed for the simultaneous impregnation system. The glass fiber enters the melting chamber through its inlet on the side surface of the nozzle, and the impregnated fibers are guided out of the nozzle and placed on the building plate. The printing speed of the samples was 10 mm/s, and the nozzle temperature and the printing bed were set to 200° C and 60 mm/s, respectively.

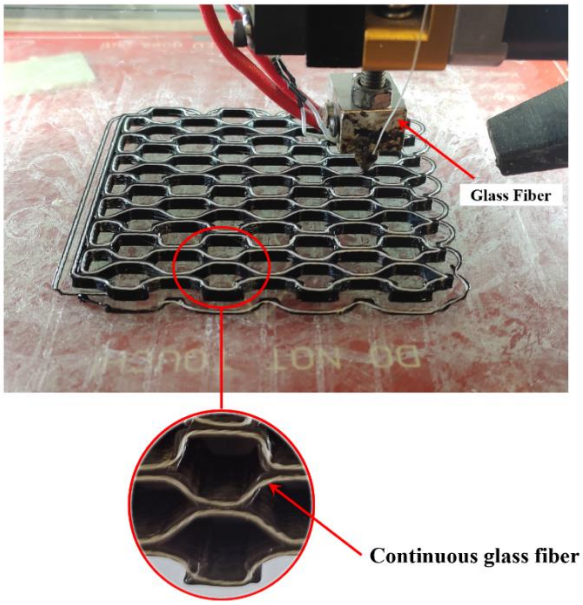

(a)

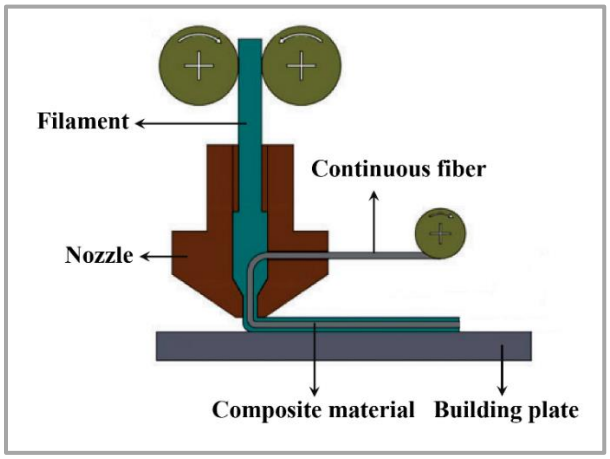

(b)

Figure 6. (a) Printing bio-inspired cellular structure with a continuous fiber, (b) Printing process[37]

4.2. Experimental test

The fiber-reinforced cellular structure was subjected to uniaxial compression testing to validate the proposed analytical model. A minimum of three samples were tested in the x and y directions (Figs.7). A SANTAM machine was used to perform the uniaxial compression testing, and a fixed crosshead speed of 5 mm/min was used. The load-displacement were obtained for analyzing, and

the nominal stress and the nominal strain were obtained to calculate modulus of elasticity. A high-resolution camera was also used to investigate the deformation and failure in samples (Fig.8). Important geometric parameters in the composite bone-inspired unite cell with 20mm×20mm×20mm dimensions are presented in Table1.

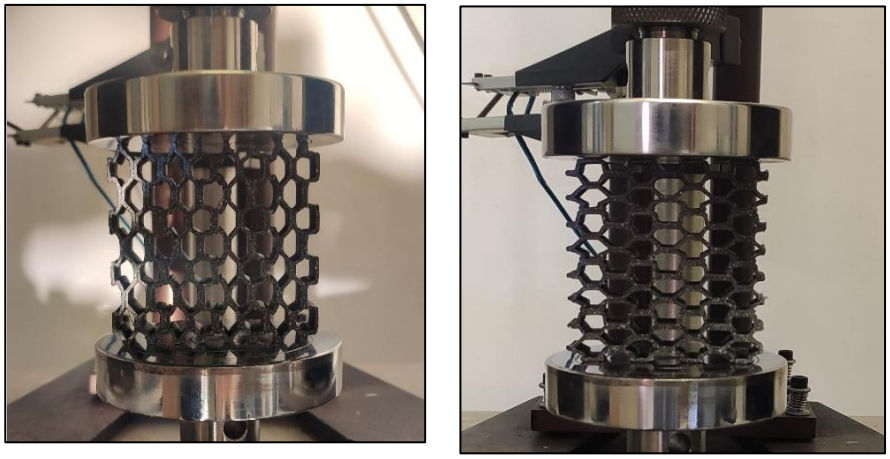

a **b**

Figure 7. (a) Compression test; x-direction, (b) y-direction

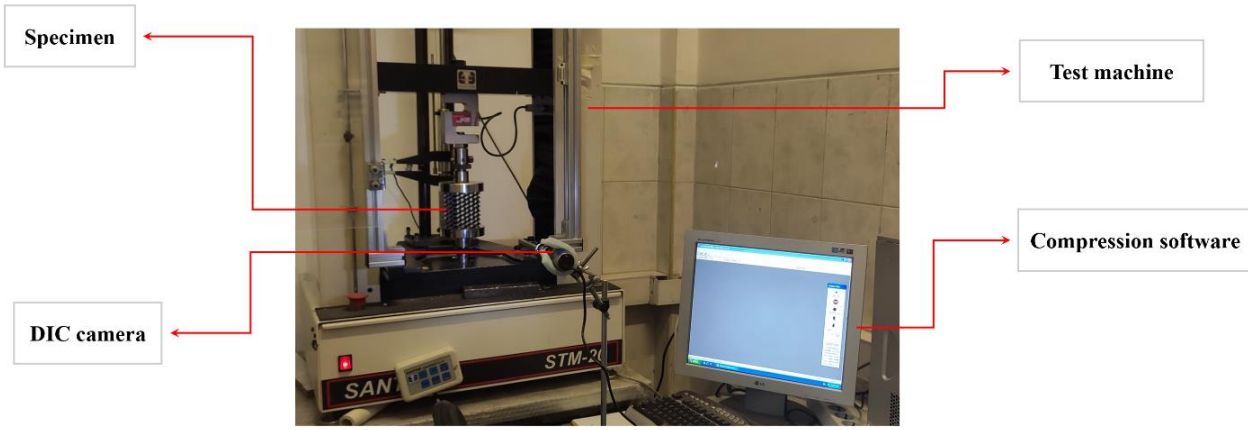

Figure 8. compression test machine with DIC camera

Table 1. Geometrical parameters of bio-inspired unit cell

variables	values	variables	Values
BC	3.8 mm	L	20 mm
CA	5 mm	W	20 mm
CK	5 mm	t	1mm
KI	5 mm	D (Extrusion depth)	20mm
KF	5 mm	α	63.43˚
FE	2.76 mm	β	25˚
FG	7.07 mm	γ	41.14˚
GJ	2.24 mm	φ_{cd}	90˚
GH	5.92mm	φ_{fg}	45˚

4.3. Digital image correlation (DIC)

Digital image correlation (DIC) is a 3D full-field, optical non-contact method to analyze the stress and strain of materials. This method compares images taken of the material before and after loading, so called reference and deformed images, respectively [40]. This technique uses a speckle pattern on the surface of material to increase the image's contrast. This method is also called digital speckle photography which is based on the computerization of the speckle pattern method by photographing a material exposed to white light in which the surface has a random speckle pattern to measure the displacement field and strain. A high-resolution camera captured the speckle pattern before and after the in-plane deformation to obtain a high-accuracy displacement field [41][42]. Various studies are utilized the DIC technique. Some studies employed this technique to obtain the stress intensity in polymeric materials such as PMMA [43]. Also, this system is used in some studies to assess Poisson's ratio of the cellular structures [1], [44] and also in biomedical research, such as crack growth in the bone [45] or mechanical properties of the cortical bone [46]. In aerospace engineering, it is performed to obtain strains and displacements in the crack growth length in the parts [47] or strain fields in carbon-epoxy composite plates [48].

In this study, the DIC technique was used to obtain Poisson's ratio by recording a speckle pattern on the surface of the bone-inspired cellular structure, as shown in Fig.9a. The speckle pattern on

the surface of the structure generated by scattering white paint. A compression test was conducted at a displacement rate of 5 mm/min and images were captured every second during the experimental procedure. All of the captured images imported in digital image analysis software GOM correlate. In this software, local deformations were calculated based on detecting the spackle pattern in two consecutive images.

The value of Poisson's ratio is estimated by defining longitudinal distance (AB) and transverse distance (CD). The elastic region was chosen to investigate the Poisson's ratio value. Fig.9b shows a typical example of images to obtain the Poisson's ratio.

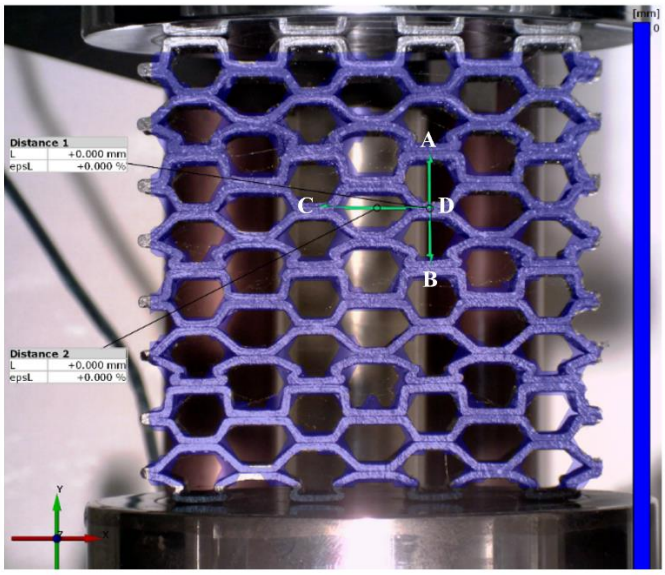

(a)

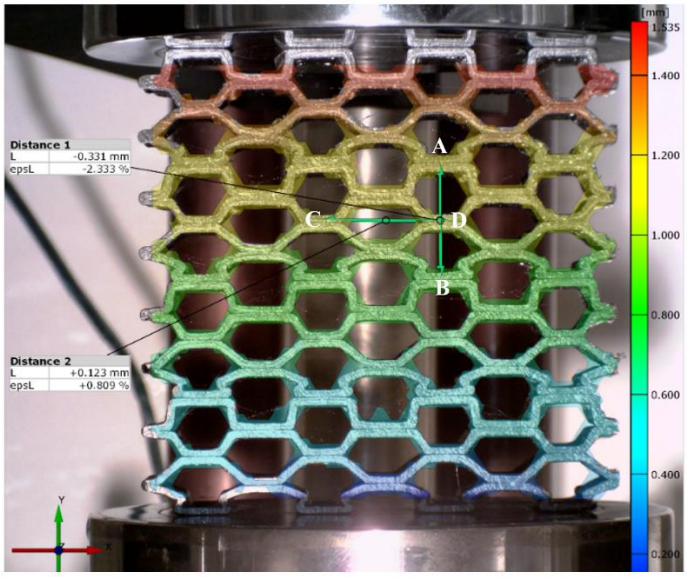

(b)

Figure 9. (a) Images processed by GOM Correlate software, the first image of strain field, (b) the image is selected for calculating Poisson's ratio

5.Finite element simulation

In this section numerical method is explained to assess mechanical properties in an orthotropic bone-inspired unit cell. ABAQUS software version 2017 was used for the simulation. Also, an explicit solver was employed in numerical simulation. The bio-inspired cellular structure was made of fiber-reinforced PLA. The orientation of the fibers in each unit cell strut was determined in the longitudinal direction of the strut. Fig.10 indicates the orientations in each strut that a local coordinate system was defined for each strut of the bone-inspired unit cell. In the defined local coordinate system, the x-axis was located along the struts and the y-axis was located perpendicular to the x-axis. The equivalent mechanical property of fiber-reinforced PLA was assigned to each strut of the unit cell.

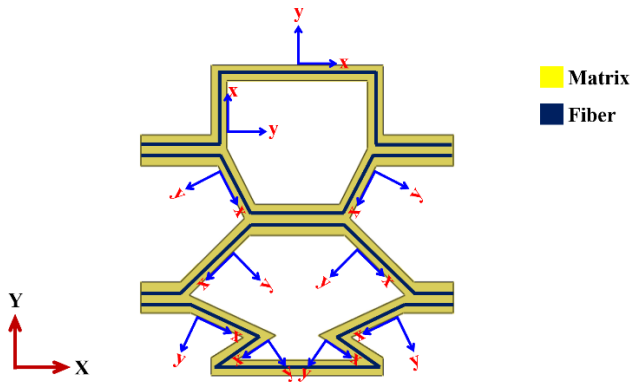

Figure 10. Fiber orientations in the bone-inspired unit cell

The proposed structure was subjected to compressive loading in both the x and y directions in the numerical analysis, and the structure was placed between two rigid plates. A displacement control condition was considered in the simulation. Boundary conditions applied to the cellular structure under loading in the y-direction are shown in Fig.11. The bottom rigid plate was completely fixed, and the upper rigid plate was set to move only in the y-direction and in other directions was set to be fixed.

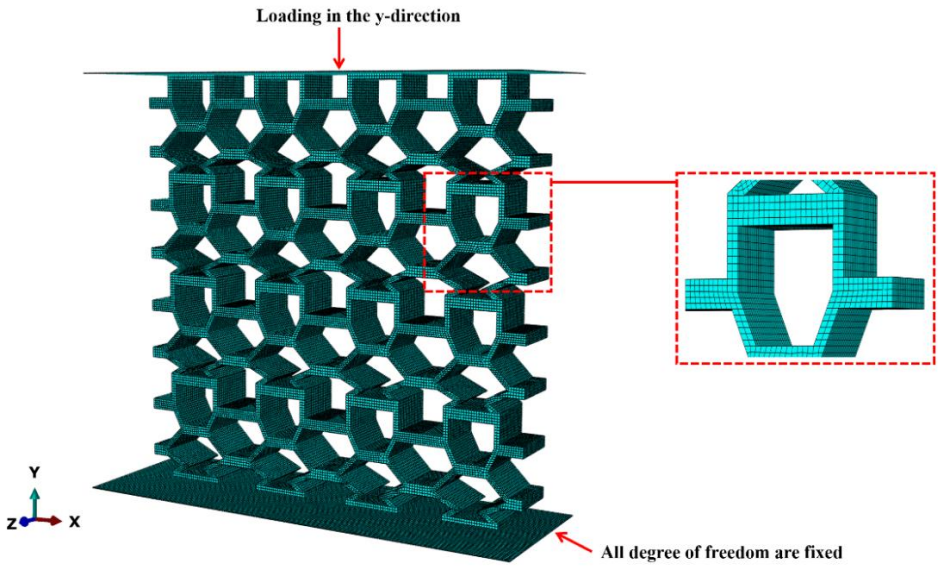

Figure 11. Boundary condition applied in numerical simulation

A mesh convergence analysis was also implemented, a mesh size of 0.5 mm was chosen, and the C3D8R element was utilized to mesh the model (Fig.11). Also, the general contact was applied to the cellular composite structures to model the structure contact behavior and contact properties were defined with a coefficient of friction equal to 0.2 for all surfaces.

For the simulation of non-linear behavior, the VUSDFLD subroutine was employed to assign the material behavior of a composite bone-inspired structure. Due to damage growth, several field variables were defined to simulate decreasing mechanical properties in the composite cellular structure. The struts of the unit cell were modeled as orthotropic material, and the ultimate tensile stress of the PLA and Fiber-reinforced PLA was chosen as 60 MPa, and 157 MPa, respectively. In the VUSDFLD subroutine, the maximum stress criteria were employed to assess decreasing mechanical properties of the fiber-reinforced bio-inspired structure. According to the assumption in this criterion, shear stress was not considered. According to this algorithm, the stress in the fiber and perpendicular to fiber directions were compared with the ultimate stresses to assign decreasing the mechanical properties in each element.

The mechanical properties of PLA and fiber-reinforced-PLA have been obtained in a previous study by current authors [49]. Due to the different filament brands used, the rule of mixture equation was used to get the E_1 property and presented in Table 2. In 3D printing processes, the parts go under the repeated cycles of heating and cooling that can lead to residual stress. In addition, the layers can have different stiffnesses due to printing parameters and the heat dissipation. It is worth noting that in this study, the effects of these parameter were considered globally and at the macro-level using 3D printing of standard tensile testing samples. These samples were used in tensile testing and the equivalent mechanical properties were assigned to the simulated model.

The numerical analysis results are used to compare with experimental and analytical results.

Table 2. Mechanical properties of the Fiber-reinforced-PLA

Specimen	E_1 (GPa)	E_2 & E_3 (GPa)	G_{12}, G_{13} & G_{23} (GPa)*	ν_{12}, ν_{13} & ν_{23}*
Fiber-reinforced-PLA	9.574	3.3	0.8	0.18

*These parameters are assumed.

6. Results and discussion

6.1. Validation of the analytical model: Experimental and Numerical

For experimental compression testing and numerical modeling, force-displacement diagrams in both directions are shown in Fig.12.

Fig.12a shows the force-displacement diagrams of the composite bone-inspired structure under loading x-direction numerically and experimentally. According to this figure in the experimental diagram, the amount of force is reached the maximum value of 4kN. After that, the force distributes almost uniformly while the structure collapses, and the plateau stress region appears. After this region the structure completely collapses, and the force increases sharply. In the numerical diagram, the amount of peak force is ~ 3.7 kN. After reaching the peak force, the plateau stress region appears which is close to the experimental diagram, and the force increases with the similar pattern to the experimental results. In general, the numerical simulation has good agreement with the experimental results in predicting the structure behavior under loading x-direction.

Fig.12b indicates the force-displacement diagrams under loading y-direction numerically and experimentally. The diagram of the experimental testing shows the amount of force reaches the maximum value of ~2kN, and after that, by collapsing the structure, the force increases upwards. The numerical simulations shows a similar trend in comparison with the experimental measurements for the peak force and the failure behavior of the structure.

In general, by comparing the results of x-direction and y-direction loading, it cand be concluded that that the composite structure has a higher amount of peak force in the x-direction, and the structure has a higher capacity to bear the loading.

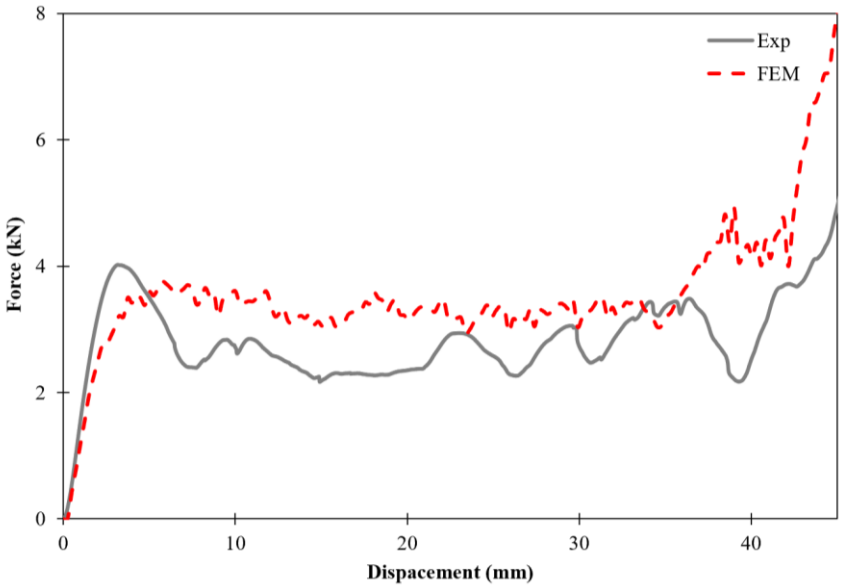

(a)

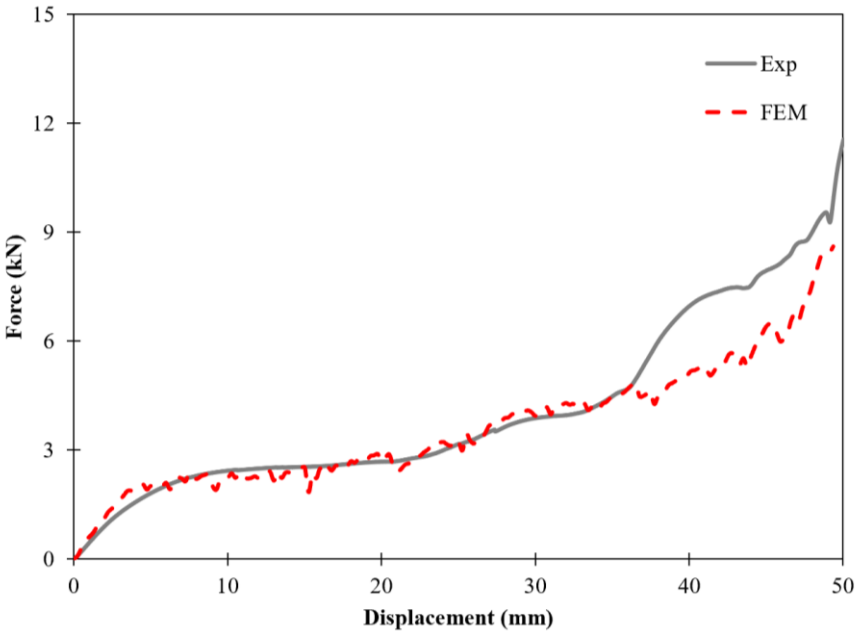

(b)

Figure 12. Force-displacement curves obtained by experimental and numerical methods, (a) under loading in the x-direction, (b) under loading in the y-direction

Energy absorption (EA) is an important parameter for assessing cellular structures. Specific Energy Absorption (SEA) of the bone-inspired unit cell with isotropic struts is compared with conventional honeycomb and re-entrant cellular structures in [30]. The results showed a 29% improvement in the energy absorption capability of the bone-inspired structure. In this study by adding the continuous glass fiber to the printed structure, the EAs at the displacement of 40mm are 108J and 122J in x and y directions, respectively. Compared to the bone-inspired unit cell with isotropic struts, the composite bioinspired structure shows a 250% improvement in energy absorption of the structure in the x-direction and an increase of 262% in energy absorption of the y-direction.

The amounts of young's modulus and Poisson's ratio have been extracted for the diagrams in both x and y directions. The gradient of force-displacement curves was used to extract young's modulus. Poisson ratio was also obtained based on DIC technique using transverse strain to axial strain. The analytical model was also used to calculate young's modulus and Poisson's ratio. Fig.13a compares young's modulus values obtained from analytical, numerical, and experimental methods. The difference between the experimental and the theoretical calculations in the x and y directions are 2.7% and 6.16%, respectively. Compared to results from the numerical modeling, the values from the analytical model show are a small difference of 1.7% in the x-direction and a moderate difference of 12% in the y-direction. These results indicate that that the developed analytical model can predict the elastic properties with high accuracy. Furthermore, Young's modulus in the x-direction is significantly higher compared to young's modulus in the y-direction. In the x-direction, fibers are oriented in the loading direction, but in the y-direction, the fibers are perpendicular to the loading direction. Therefore, the amount of stiffness in the x-direction is significantly higher compared to the y-direction.

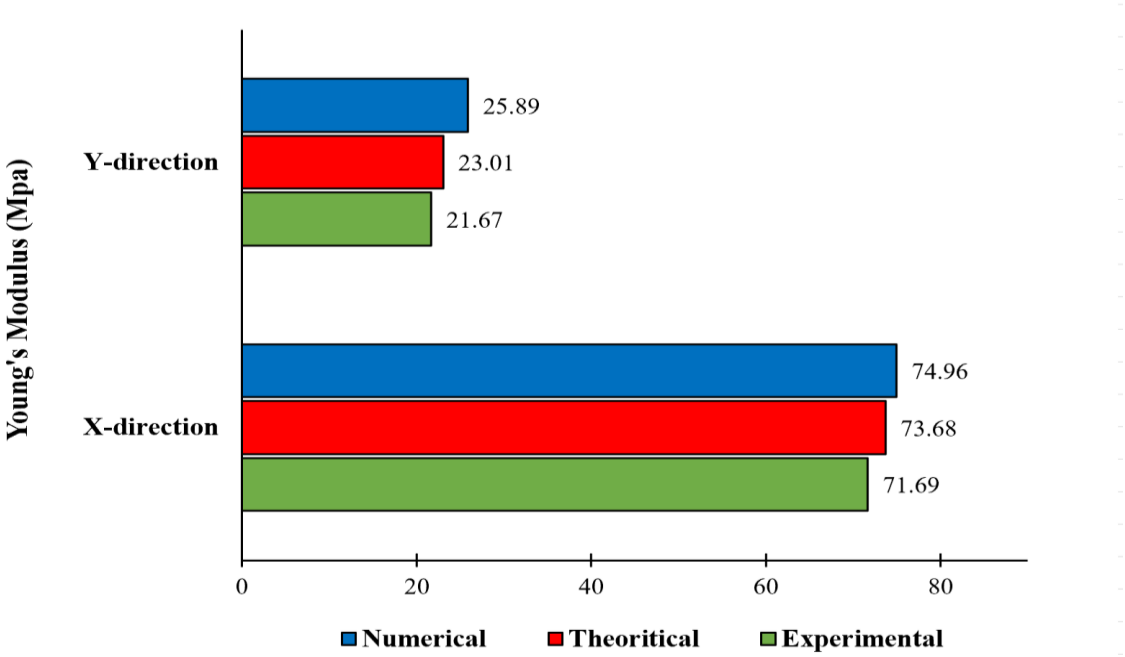

(a)

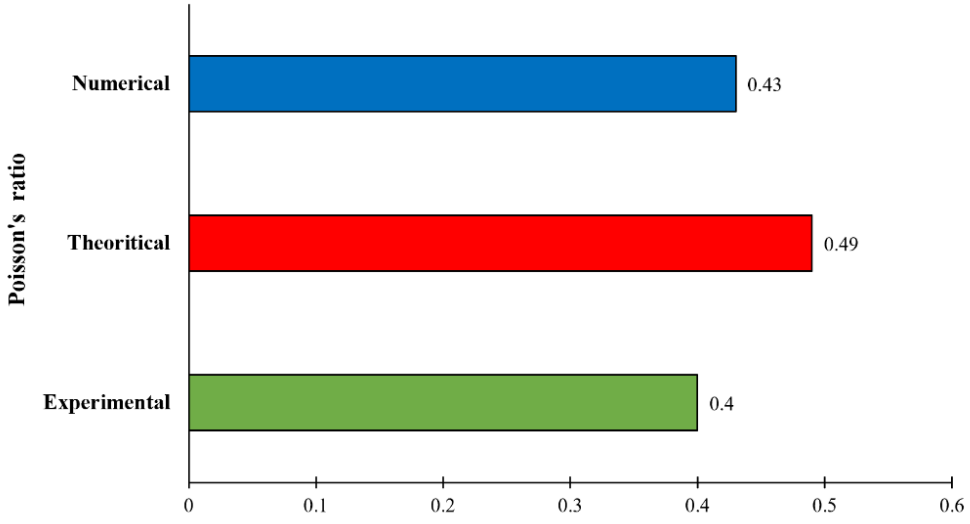

(b)

Figure 13. Comparison between the theoretical and experimental test; (a) Young's modulus, (b) Poisson's ratio

Fig.13b compares the values of Poisson's ratio (υ_{xy}) obtained from the analytical calculation, numerical modeling and experimental measurements using DIC technique. The calculated Poisson's ratio from the analytical method shows a moderate difference of 12% compared to the

results obtained from the numerical modeling. However, there is a large difference of 20% between the experimental and the calculated Poisson's ratio from the analytical method. Poisson's ratio has a high sensitivity to the angles of cells [50]. It is very difficult to manufacture the angles and their dimensions the same as the ones used in the modeling. Thus, they cause differences between the experimental and numerical results.

The numerical modeling has been used to investigate the effect of adding fiber on mechanical properties of cellular structures. Fig.14 compares young's modulus of the bio-inspired cellular structures for a glass fiber-reinforced PLA (continuous glass fiber) and a pure PLA.

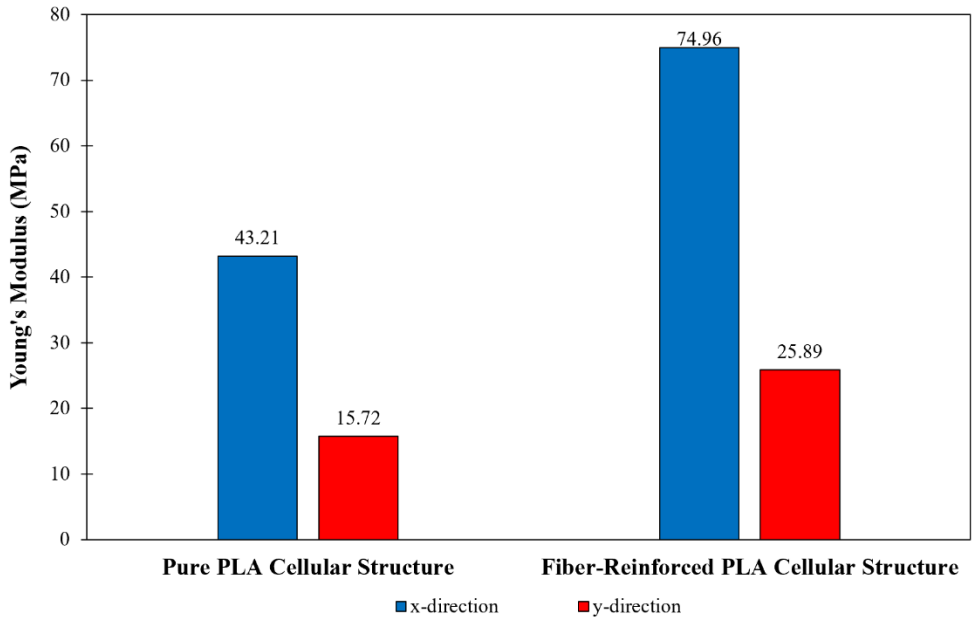

Figure 14. Effect of fiber in elastic properties in x and y directions

In the orthotropic honeycomb structure, young's modulus in the x and y directions are increased by 73% and 64%, respectively for a glass fiber-reinforced PLA. Therefore, continuous glass fiber plays an effective role on the enhancement of the mechanical properties of the bone-inspired unit cell.

6.2. Parametric study

For a composite bio-inspired unit cell, the effects of geometrical parameters (as shown in Fig.2) on elastic modulus and Poisson's ratio have been studied in both x and y directions. These properties have been investigated based on effective angles and lengths. The unit cell with the geometrical parameters of Table 1 is selected for the parametric study.

Figs.15 shows the effect of unit cell geometrical parameters on the elastic modulus in the x-direction. Fig.15a displays the effect of changes of B_1 and B_2 on the elastic modulus. This parametric study only considered B_1 and B_2, and other parameters have constant values, according to Table 1. In this Figure with increasing B_1 and B_2, the elastic modulus decreases. In Fig. 15b, B_1 and β are considered and other geometrical parameters are constant. This figure shows with increasing the angle β, the elastic modulus decreases, and with increasing B_1, the elastic modulus is almost constant and slightly decreases. In the Fig.15c, B_1 and γ are considered and values of the other parameters are constant. This figure shows that when angle γ increases, the amount of elastic modulus decreases, and with increasing B_1 value, the elastic modulus is almost constant and decreases slightly. Fig.15d illustrates that as β and γ increase the elastic modulus decrease. In these parametric diagrams, β and γ are considered and other geometrical parameters of the unit cell are constant.

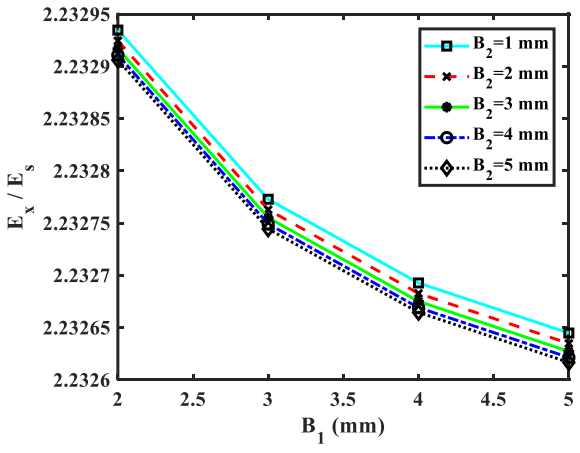

(a)

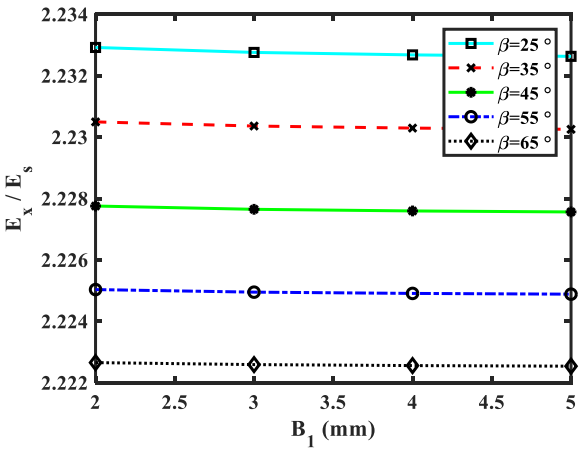

(b)

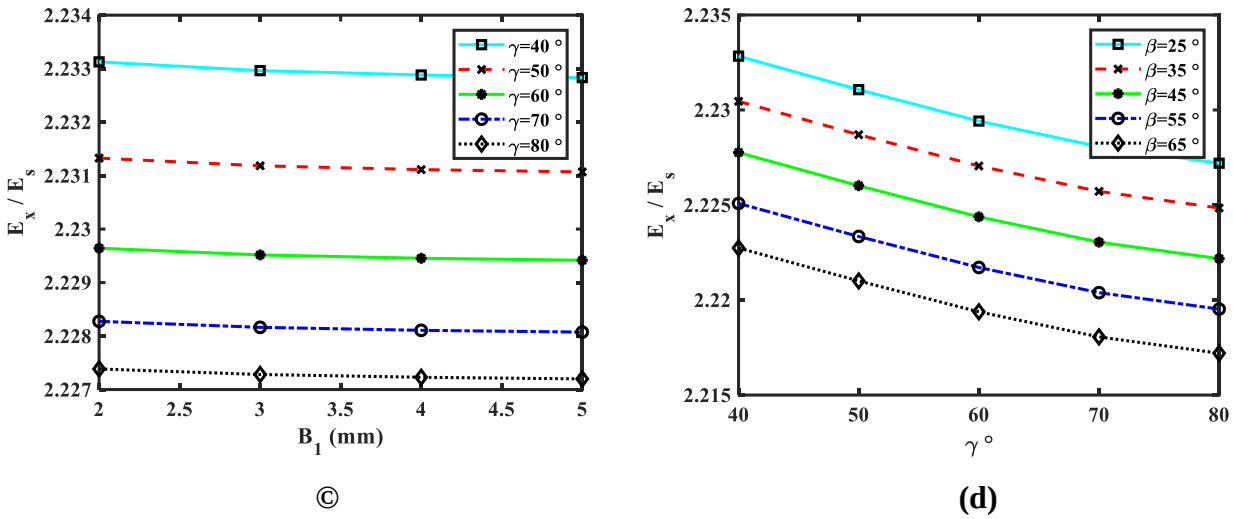

Figure 15. Effect of changes of a unit cell parameter on the elastic modulus in the x-direction.

Figs.16 shows the effect of unit cell geometrical parameters on the elastic modulus in the y-direction. Fig.16a displays the effect of changes of B_1 and β on the elastic modulus. According to the obtained results, the elastic modulus increased with enhancing the values of B_1 and slightly decreased with reducing the value of B_1. In these parametric diagrams, B_1 and β are considered and other parameters have constant values, according to Table 1. Fig. 16b indicates that with increasing the value of B_1 and B_2, the elastic modulus decreases. Effect of B_1 and B_2 is assessed in this figure and other parameters have constant values. Fig.16c shows that the elastic modulus increases with increasing the value of α and γ angles. α and γ angles only considered in this study and other geometrical parameters have constant values. In Fig.16d, the effect of α and β is investigated and other parameters of the unit cell are considered constant values. This figure illustrates the effect of changes of α and β on the elastic modulus. The elastic modulus increased with enhancing the value of α and β angles.

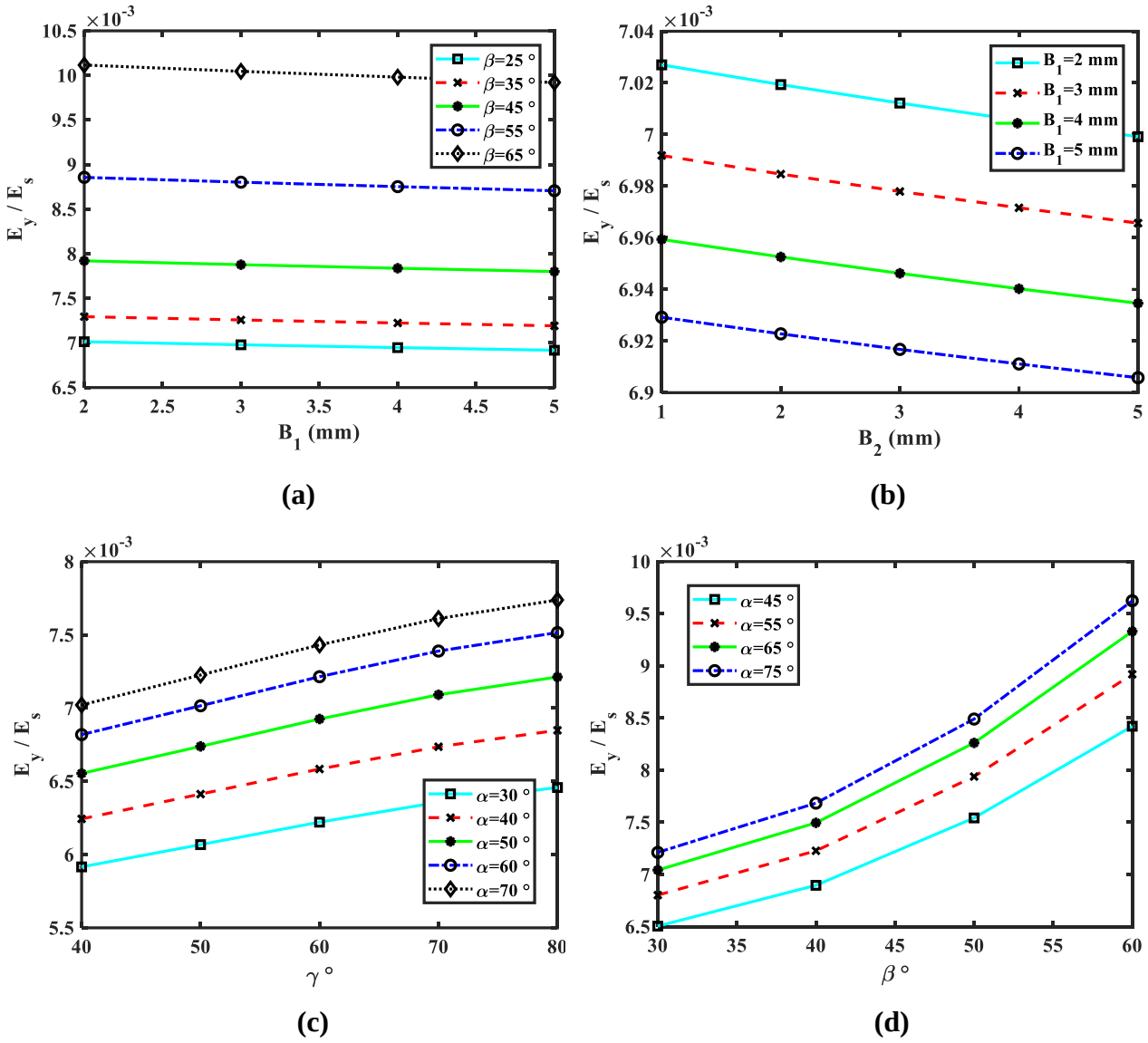

Figure 16. Effect of changes of a unit cell parameter on the elastic modulus in the y-direction.

Figs.17 shows the effect of unit cell geometrical parameters on the elastic modulus in the y/x-directions. In Fig.17a shows that with increasing the α angle, E_y/E_x enhances, while there is no change in E_x/E_y by changing B_2. In this parametric study, only the effect of B_2 and α are considered and other parameters are constant. Fig.17b indicates that with increasing the γ and α angles, the elastic modulus increases. This figure investigates the effect of γ and α angles on the elastic modulus. Fig. 17c shows that increasing the value of α and γ angles results in the enhancement in the elastic modulus. In this figure, only α and γ angles are considered. Fig.17d

illustrates that the elastic modulus raises with increasing the value of α and β angles and other geometrical parameters are considered constant.

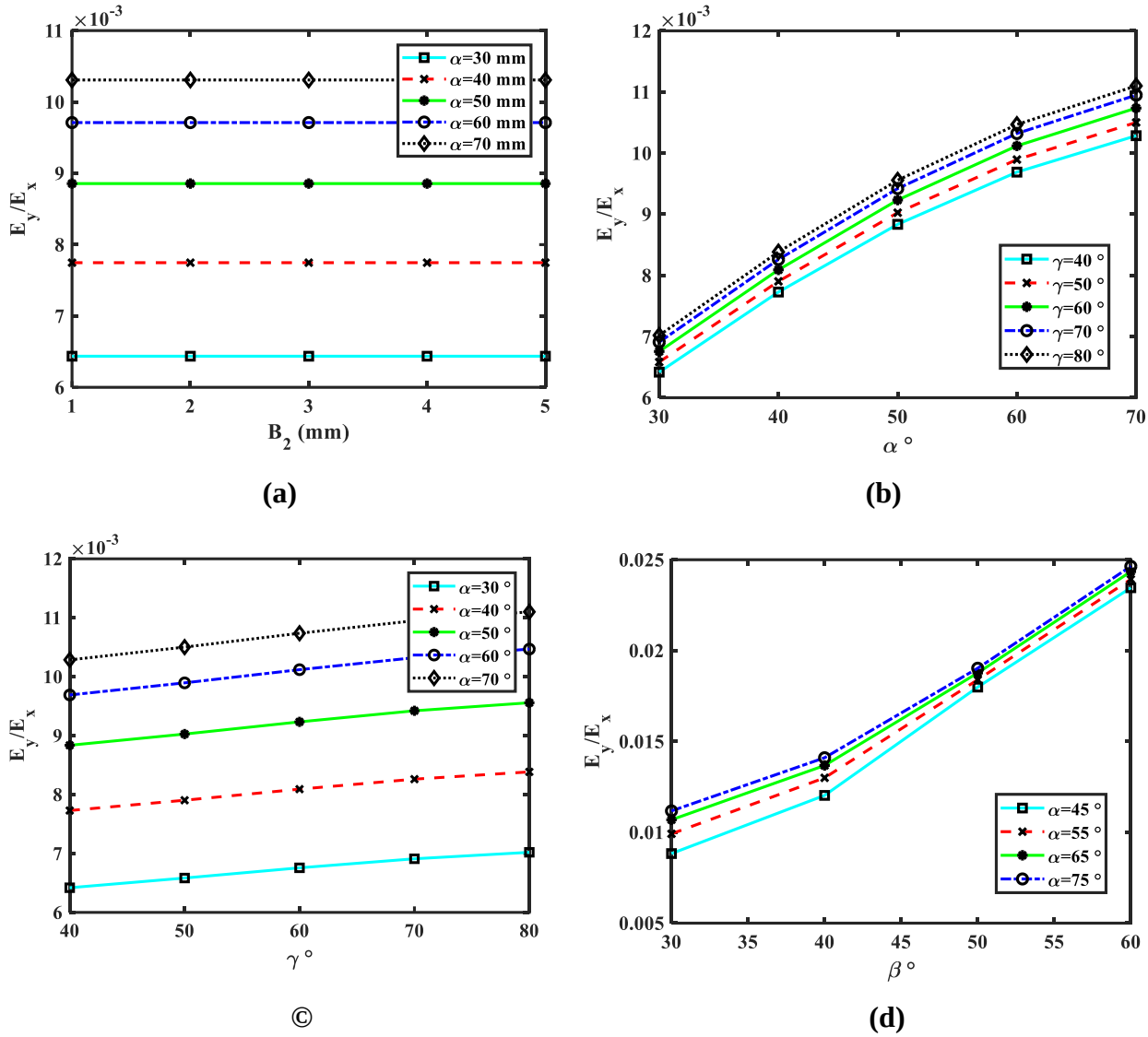

Figure 17. Effect of changes of a unit cell parameter on the elastic modulus in the y/x direction.

Figs.18 demonstrates the effect of geometric parameters on the Pois'on's ratio. Fig.18a shows that with increasing B_2 the Pois'on's ratio increases while by increasing the value of B_1 the Pois'on's ratio decreases. Other geometrical parameters of the unit cell are considered constant value, according to Table 1. Fig. 18b displays that the value of Poisson's ratio increases with increasing the value of α , while it decreases with increasing the value of B_1. In this parametric study, only α and B_1 are considered. Fig. 18c shows that with increasing the both angles the

Poisson's ratio increases and other geometrical parameters in the bio-inspired unit cell have constant values. In Fig.18d, it is obvious with increasing the α and β angle the value of Poisson's ratio increases. α and β angles are only considered and other parameters are assumed constant.

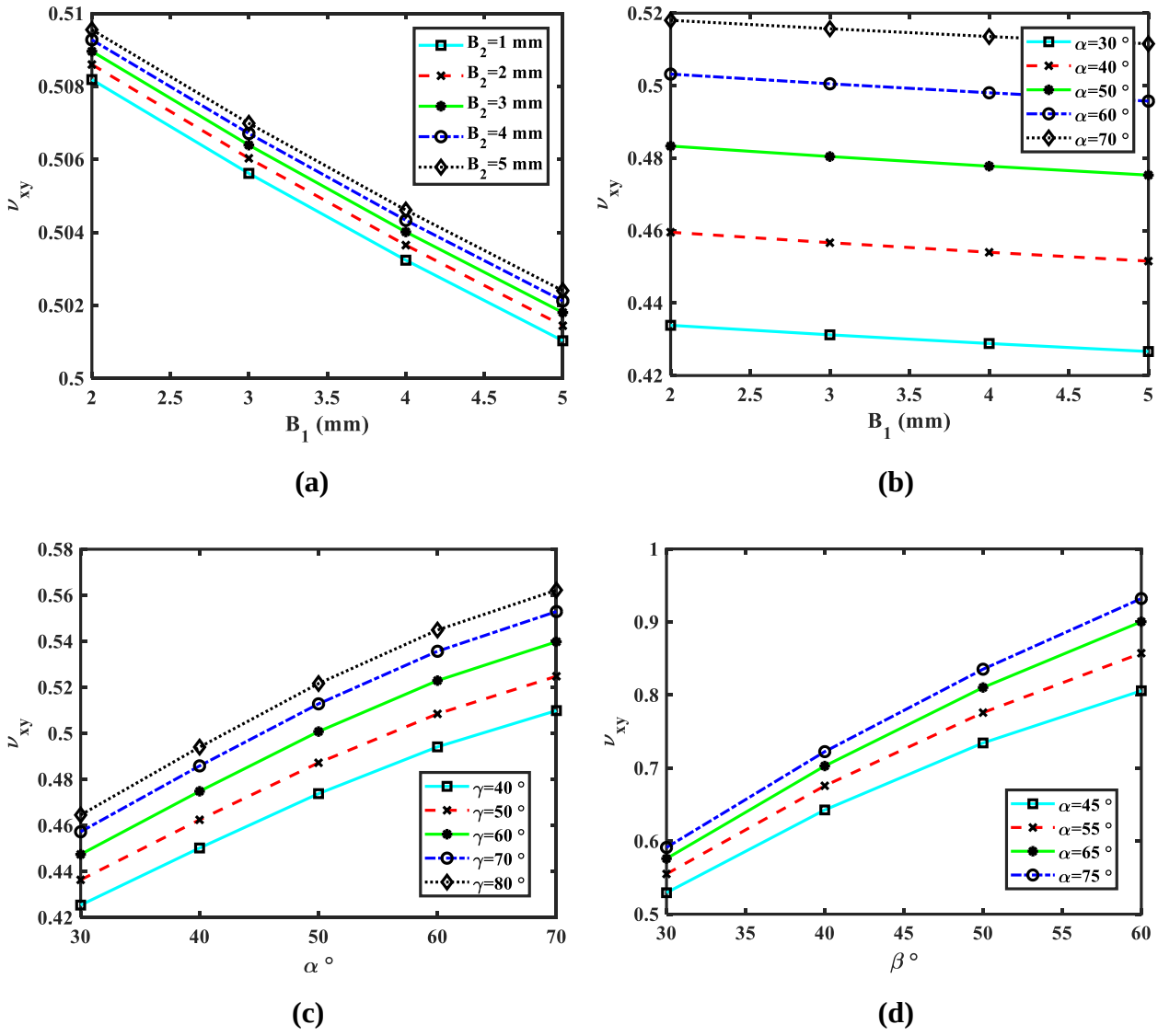

Figure 18. Effect of changes of a unit cell parameter on the Poisson's ratio.

Conclusion

In this study, the total strain energy in an orthotropic ply is obtained by using classical lamination theory (CLT) to evaluate the mechanical properties in the proposed orthotropic cellular structure. Subsequently, Castigliano's second theorem was used to calculate the elastic properties in both x and y directions. Composite bio-inspired cellular structures were made using an FDM 3D printing method and subjected to a compression test to validate the proposed analytical model. The DIC technique was also implemented to estimate Poisson's ratio by measuring strain and displacement contours. The results of the theoretical model and experimental tests showed a good agreement. Numerical simulations have also been employed for further studies. The numerical analysis showed that the amount of stiffness in the x-direction in the fiber-reinforced cellular structure has increased by 73% compared to the structure without fiber. In addition, the amount of stiffness in the y-direction in the fiber-reinforced cellular structure has increased by 64% compared to the structure without fiber. Finally, a parametric study was performed to investigate the effects of geometric parameters on the mechanical properties. The bio-inspired cellular structure has various geometrical parameters. Therefore, the proposed analytical model can be utilized to optimize cellular structures for various applications such as energy absorber structures in vehicles or bio-implant designs using biomaterials.

References

[1] M. Sadeghzade, H. Gharehbaghi, and A. Farrokhabadi, “Experimental and analytical studies of mechanical properties of additively manufactured lattice structure based on octagonal bipyramid cubic unit cell,” *Addit. Manuf.*, vol. 48, no. PB, p. 102403, 2021, doi: 10.1016/j.addma.2021.102403.

[2] H. Gharehbaghi, M. Sadeghzade, and A. Farrokhabadi, “Introducing the new lattice structure based on the representative element double octagonal bipyramid,” *Aerosp. Sci. Technol.*, vol. 121, p. 107383, 2022, doi: https://doi.org/10.1016/j.ast.2022.107383.

[3] A. Alomarah, S. H. Masood, I. Sbarski, B. Faisal, Z. Gao, and D. Ruan, “Compressive properties of 3D printed auxetic structures: experimental and numerical studies,” *Virtual Phys. Prototyp.*, vol. 15, no. 1, pp. 1–21, 2020, doi: 10.1080/17452759.2019.1644184.

[4] V. Kumar, G. Manogharan, and D. R. Cormier, “Design of periodic cellular structures for heat exchanger applications,” *20th Annu. Int. Solid Free. Fabr. Symp. SFF 2009*, no. December 2015, pp. 738–748, 2009.

[5] W. Yang, J. An, C. K. Chua, and K. Zhou, “Acoustic absorptions of multifunctional

polymeric cellular structures based on triply periodic minimal surfaces fabricated by stereolithography," *Virtual Phys. Prototyp.*, vol. 15, no. 2, pp. 242–249, 2020, doi: 10.1080/17452759.2020.1740747.

[6] F. Scarpa, M.-A. Boucher, C. Smith, R. Rajasekaran, and K. Evans, "Effective topologies for vibration damping inserts in honeycomb structures," *Compos. Struct.*, vol. 106, Dec. 2013, doi: 10.1016/j.compstruct.2013.05.036,.

[7] K. M. Abate, A. Nazir, J. E. Chen, and J. Y. Jeng, "Design, optimization, and evaluation of additively manufactured vintiles cellular structure for acetabular cup implant," *Processes*, vol. 8, no. 1, 2020, doi: 10.3390/pr8010025.

[8] M. Naghavi Zadeh, I. Dayyani, and M. Yasaee, "Fish Cells, a new zero Poisson's ratio metamaterial—Part I: Design and experiment," *J. Intell. Mater. Syst. Struct.*, vol. 31, no. 13, pp. 1617–1637, 2020, doi: 10.1177/1045389X20930079.

[9] M. N. Zadeh, I. Dayyani, and M. Yasaee, "Fish Cells, a new zero Poisson's ratio metamaterial—part II: Elastic properties," *J. Intell. Mater. Syst. Struct.*, vol. 31, no. 19, pp. 2196–2210, 2020, doi: 10.1177/1045389X20942576.

[10] S. Babaee, B. H. Jahromi, A. Ajdari, H. Nayeb-Hashemi, and A. Vaziri, "Mechanical properties of open-cell rhombic dodecahedron cellular structures," *Acta Mater.*, vol. 60, no. 6–7, pp. 2873–2885, 2012, doi: 10.1016/j.actamat.2012.01.052.

[11] E. Harkati, N. Daoudi, A. Bezazi, A. Haddad, and F. Scarpa, "In-plane elasticity of a multi re-entrant auxetic honeycomb," *Compos. Struct.*, vol. 180, no. November 2018, pp. 130–139, 2017, doi: 10.1016/j.compstruct.2017.08.014.

[12] C. Lira, P. Innocenti, and F. Scarpa, "Transverse elastic shear of auxetic multi re-entrant honeycombs," *Compos. Struct.*, vol. 90, no. 3, pp. 314–322, 2009, doi: 10.1016/j.compstruct.2009.03.009.

[13] I. G. Masters and K. E. Evans, "Models for the elastic deformation of honeycombs," *Compos. Struct.*, vol. 35, no. 4, pp. 403–422, 1996, doi: 10.1016/S0263-8223(96)00054-2.

[14] Z. X. Lu, X. Li, Z. Y. Yang, and F. Xie, "Novel structure with negative Poisson's ratio and enhanced Young's modulus," *Compos. Struct.*, vol. 138, pp. 243–252, 2016, doi: 10.1016/j.compstruct.2015.11.036.

[15] W. Liu, H. Li, and J. Zhang, "Elastic properties of a cellular structure with in-plane corrugated cosine beams," *Compos. Struct.*, vol. 180, pp. 251–262, 2017, doi: 10.1016/j.compstruct.2017.08.022.

[16] J. Rong and L. Zhou, "Design of flexible skin based on a mixed cruciform honeycomb," in *Proc.SPIE*, Apr. 2017, vol. 10168, doi: 10.1117/12.2258579.

[17] X. Li, Q. Wang, Z. Yang, and Z. Lu, "Novel auxetic structures with enhanced mechanical properties," *Extrem. Mech. Lett.*, vol. 27, pp. 59–65, 2019, doi: 10.1016/j.eml.2019.01.002.

[18] R. Torre and S. Brischetto, "Experimental characterization and finite element validation of orthotropic 3D-printed polymeric parts," *Int. J. Mech. Sci.*, vol. 219, p. 107095, 2022, doi:

https://doi.org/10.1016/j.ijmecsci.2022.107095.

[19] R. Oftadeh, B. Haghpanah, J. Papadopoulos, A. M. S. Hamouda, H. Nayeb-Hashemi, and A. Vaziri, “Mechanics of anisotropic hierarchical honeycombs,” *Int. J. Mech. Sci.*, vol. 81, pp. 126–136, 2014, doi: 10.1016/j.ijmecsci.2014.02.011.

[20] W. Liu, H. Li, Z. Yang, J. Zhang, and X. Ge, “In-plane elastic properties of a 2D chiral cellular structure with V-shaped wings,” *Eng. Struct.*, vol. 210, no. 8, p. 110384, 2020, doi: 10.1016/j.engstruct.2020.110384.

[21] J. Huang, X. Gong, Q. Zhang, F. Scarpa, Y. Liu, and J. Leng, “In-plane mechanics of a novel zero Poisson’s ratio honeycomb core,” *Compos. Part B Eng.*, vol. 89, pp. 67–76, 2016, doi: 10.1016/j.compositesb.2015.11.032.

[22] N. Wang and Q. Deng, “Effect of Axial Deformation on Elastic Properties of Irregular Honeycomb Structure,” *Chinese J. Mech. Eng. (English Ed.*, vol. 34, no. 1, 2021, doi: 10.1186/s10033-021-00574-3.

[23] T. Mukhopadhyay and S. Adhikari, “Effective in-plane elastic properties of auxetic honeycombs with spatial irregularity,” *Mech. Mater.*, vol. 95, pp. 204–222, 2016, doi: 10.1016/j.mechmat.2016.01.009.

[24] W. Liu, H. Li, Z. Yang, J. Zhang, and C. Xiong, “Mechanics of a novel cellular structure for morphing applications,” *Aerosp. Sci. Technol.*, vol. 95, p. 105479, 2019, doi: 10.1016/j.ast.2019.105479.

[25] C. Structures, “Gong , X ., Huang , J ., Scarpa , F ., Liu , Y ., & Leng , J . (2015). Zero Poisson ’ s ratio cellular structure for two-dimensional morphing,” pp. 384–392, 2015.

[26] S. Balawi and J. L. Abot, “A refined model for the effective in-plane elastic moduli of hexagonal honeycombs,” *Compos. Struct.*, vol. 84, no. 2, pp. 147–158, 2008, doi: 10.1016/j.compstruct.2007.07.009.

[27] E. H. Harkati, N. E. H. Daoudi, C. E. Abaidia, A. Bezazi, and F. Scarpa, “The Elastic Uniaxial Properties of a Center Symmetric Honeycomb with Curved Cell Walls: Effect of Density and Curvature,” *Phys. Status Solidi Basic Res.*, vol. 254, no. 12, 2017, doi: 10.1002/pssb.201600818.

[28] Q. Gao, W. H. Liao, and L. Wang, “An analytical model of cylindrical double-arrowed honeycomb with negative Poisson’s ratio,” *Int. J. Mech. Sci.*, vol. 173, p. 105400, 2020, doi: 10.1016/j.ijmecsci.2019.105400.

[29] A. Ghazlan, T. Ngo, T. Nguyen, S. Linforth, and T. Van Le, “Uncovering a high-performance bio-mimetic cellular structure from trabecular bone,” *Sci. Rep.*, vol. 10, no. 1, pp. 1–13, 2020, doi: 10.1038/s41598-020-70536-7.

[30] A. Ghazlan, T. Nguyen, T. Ngo, S. Linforth, and V. T. Le, “Performance of a 3D printed cellular structure inspired by bone,” *Thin-Walled Struct.*, vol. 151, no. August 2019, p. 106713, 2020, doi: 10.1016/j.tws.2020.106713.

[31] R. Hedayati, N. Ghavidelnia, M. Sadighi, and M. Bodaghi, “Improving the accuracy of analytical relationships for mechanical properties of permeable metamaterials,” *Appl. Sci.*,

vol. 11, no. 3, pp. 1–38, 2021, doi: 10.3390/app11031332.

[32] R. Torre, S. Brischetto, and I. R. Dipietro, "Buckling developed in 3D printed PLA cuboidal samples under compression: Analytical, numerical and experimental investigations," *Addit. Manuf.*, vol. 38, no. November 2020, p. 101790, 2021, doi: 10.1016/j.addma.2020.101790.

[33] C. Quan, B. Han, Z. Hou, Q. Zhang, X. Tian, and T. J. Lu, "3D Printed Continuous Fiber Reinforced Composite Auxetic Honeycomb Structures," *Compos. Part B Eng.*, vol. 187, no. February, p. 107858, 2020, doi: 10.1016/j.compositesb.2020.107858.

[34] H. Veisi and A. Farrokhabadi, "Investigation of the equivalent material properties and failure stress of the re-entrant composite lattice structures using an analytical model," *Compos. Struct.*, vol. 257, no. September, p. 113161, 2021, doi: 10.1016/j.compstruct.2020.113161.

[35] A. Farrokhabadi, M. M. Ashrafian, H. Gharehbaghi, and R. Nazari, "Evaluation of the equivalent mechanical properties in a novel composite cruciform honeycomb using analytical and numerical methods," *Compos. Struct.*, vol. 275, p. 114410, 2021, doi: https://doi.org/10.1016/j.compstruct.2021.114410.

[36] A. Farrokhabadi, M. M. Ashrafian, and M. Fotouhi, "Design and characterization of an orthotropic accordion cellular honeycomb as one-dimensional morphing structures with enhanced properties," *J. Sandw. Struct. Mater.*, p. 10996362211070248, Jan. 2022, doi: 10.1177/10996362211070249.

[37] B. Akhoundi, A. H. Behravesh, and A. Bagheri Saed, "Improving mechanical properties of continuous fiber-reinforced thermoplastic composites produced by FDM 3D printer," *J. Reinf. Plast. Compos.*, vol. 38, no. 3, pp. 99–116, 2019, doi: 10.1177/0731684418807300.

[38] A. Antolak-Dudka *et al.*, "Static and dynamic loading behavior of Ti6Al4V honeycomb structures manufactured by Laser Engineered Net Shaping (LENSTM) technology," *Materials (Basel).*, vol. 12, no. 8, 2019, doi: 10.3390/ma12081225.

[39] P. Płatek *et al.*, "Deformation process of 3D printed structures made from flexible material with different values of relative density," *Polymers (Basel).*, vol. 12, no. 9, 2020, doi: 10.3390/POLYM12092120.

[40] P. C. Hung and A. S. Voloshin, "In-plane strain measurement by digital image correlation," *J. Brazilian Soc. Mech. Sci. Eng.*, vol. 25, no. 3, pp. 215–221, 2003, doi: 10.1590/S1678-58782003000300001.

[41] M. A. Sutton, "Computer vision-based, noncontacting deformation measurements in mechanics: A generational transformation," *Appl. Mech. Rev.*, vol. 65, no. 5, 2013, doi: 10.1115/1.4024984.

[42] M. Sutton, W. Wolters, W. Peters, W. Ranson, and S. McNeill, "Determination of displacements using an improved digital correlation method," *Image Vis. Comput.*, vol. 1, no. 3, pp. 133–139, 1983, doi: 10.1016/0262-8856(83)90064-1.

[43] S. R. McNeill, W. H. Peters, and M. A. Sutton, "Estimation of stress intensity factor by digital image correlation," *Eng. Fract. Mech.*, vol. 28, no. 1, pp. 101–112, 1987, doi:

https://doi.org/10.1016/0013-7944(87)90124-X.

[44] S. Linforth, T. Ngo, P. Tran, D. Ruan, and R. Odish, “Investigation of the auxetic oval structure for energy absorption through quasi-static and dynamic experiments,” *Int. J. Impact Eng.*, vol. 147, no. October, 2021, doi: 10.1016/j.ijimpeng.2020.103741.

[45] B. An, Y. Liu, D. Arola, and D. Zhang, “Fracture toughening mechanism of cortical bone: An experimental and numerical approach,” *J. Mech. Behav. Biomed. Mater.*, vol. 4, pp. 983–992, 2011, doi: 10.1016/j.jmbbm.2011.02.012.

[46] T. Tang, V. Ebacher, P. Cripton, P. Guy, H. McKay, and R. Wang, “Shear deformation and fracture of human cortical bone,” *Bone*, vol. 71, pp. 25–35, 2015, doi: https://doi.org/10.1016/j.bone.2014.10.001.

[47] M. A. Sutton, S. R. McNeill, J. D. Helm, and M. L. Boone, “Measurement of Crack Tip Opening Displacement and Full-field Deformations During Fracture of Aerospace Materials Using 2D and 3D Image Correlation Methods,” in *IUTAM Symposium on Advanced Optical Methods and Applications in Solid Mechanics*, 2002, pp. 571–580.

[48] M. A. Caminero, M. Lopez-Pedrosa, C. Pinna, and C. Soutis, “Damage monitoring and analysis of composite laminates with an open hole and adhesively bonded repairs using digital image correlation,” *Compos. Part B Eng.*, vol. 53, pp. 76–91, 2013, doi: https://doi.org/10.1016/j.compositesb.2013.04.050.

[49] A. Farrokhabadi, H. Veisi, H. Gharehbaghi, J. Montesano, A. H. Behravesh, and S. K. Hedayati, “Investigation of the energy absorption capacity of foam-filled 3D-printed glass fiber reinforced thermoplastic auxetic honeycomb structures,” *Mech. Adv. Mater. Struct.*, pp. 1–12, Feb. 2022, doi: 10.1080/15376494.2021.2023919.

[50] M. J. Khoshgoftar and A. Barkhordari, “Sensitivity analysis and study of parameters affecting auxetic cells with reentrant cell structure,” *Mater. Today Commun.*, vol. 31, p. 103786, 2022, doi: https://doi.org/10.1016/j.mtcomm.2022.103786.